ADVANCED FUNCTIONAL MATERIALS
www.afm-journal.de

Unveiling the Nanoparticle-Seeded Catalytic Nucleation Kinetics of Perovskite Solar Cells by Time-Resolved GIXS

Chung-Yao Lin, Shao-Sian Li, Je-Wei Chang, Hao-Chung Chia, Yu-Yun Hsiao, Chun-Jen Su, Bing-Jun Lian, Cheng-Yen Wen, Shao-Ku Huang, Wei-Ru Wu, Di-Yan Wang, An-Chung Su, Chun-Wei Chen, and U-Ser Jeng**

Recently, a new seeding growth approach for perovskite thin films is reported to significantly enhance the device performance of perovskite solar cells. This work unveils the intermediate structures and the corresponding growth kinetics during conversion to perovskite crystal thin films assisted by seeding PbS nanocrystals (NCs), using time-resolved grazing-incidence X-ray scattering. Through analyses of time-resolved crystal formation kinetics obtained from synchrotron X-rays with a fast subsecond probing time resolution, an important "catalytic" role of the seed-like PbS NCs is clearly elucidated. The perovskite precursor-capped PbS NCs are found to not only accelerate the nucleation of a highly oriented intermediate phase, but also catalyze the conversion of the intermediate phase into perovskite crystals with a reduced activation energy E_a = 47 (±5) kJ mol^{-1}, compared to 145 (±38) kJ mol^{-1} for the pristine perovskite thin film. The reduced E_a is attributed to a designated crystal lattice alignment of the perovskite nanocrystals with perovskite cubic crystals; the pivotal heterointerface alignment of the perovskite crystals coordinated by the Pb NCs leads to an improved film surface morphology with less pinholes and enhanced crystal texture and thermal stability. These together contribute to the significantly improved photovoltaic performance of the corresponding devices.

1. Introduction

Remarkable progress in the field of organic–inorganic halide perovskite solar cells, with a rapid increase in the power conversion efficiencies (PCEs) of over 20%, has been achieved in the past few years.[1–4] The key strategy to obtain high-performance perovskite solar cells is to fabricate high-quality films with controllable morphologies comprising good crystallinity with texture, minimum pinholes, and high surface coverage, using solution processing.[1–4] Many methods, such as thermal annealing,[5] solvent engineering,[6,7] and incorporating chemical additives,[8] have been demonstrated to enhance the PCEs of perovskite solar cells by improving their morphology and crystallinity. These techniques have a significant impact on the enhanced PCE of perovskite solar cell devices in the past few years.[9] Recently, a new approach called the intermixing-seeded growth technique was reported to significantly enhance the device performance of perovskite solar cells by including a small amount of seed-like precursor-capped PbS nanoparticles during film growth.[10] Through interfacial engineering with ligand-exchange treatment, the MAI-capped PbS nanoparticles, intermixed with the perovskite-precursor solution, could function as effective heterogeneous nucleation sites to promote the formation of the inorganic framework of perovskite lattice structures.[10] Unlike the conventional chemical additive in the fabrication of perovskite thin films,[11] such heterogeneous nucleation of perovskite crystals seeded with

C.-Y. Lin, J.-W. Chang, H.-C. Chia, B.-J. Lian, Prof. A.-C. Su, Prof. U.-S. Jeng
Department of Chemical Engineering
National Tsing Hua University
Hsinchu 30013, Taiwan
E-mail: usjeng@nsrrc.org.tw
Prof. S.-S. Li
Graduate Institute of Biomedical Optomechatronics
Taipei, Medical University
Taipei 11031, Taiwan
Y.-Y. Hsiao, Prof. C.-Y. Wen, S.-K. Huang, Prof. C.-W. Chen
Department of Materials Science and Engineering
National Taiwan University
Taipei 10617, Taiwan
E-mail: chunwei@ntu.edu.tw
The ORCID identification number(s) for the author(s) of this article can be found under https://doi.org/10.1002/adfm.201902582.
Dr. C.-J. Su, W.-R. Wu, Prof. U.-S. Jeng
National Synchrotron Radiation Research Center
Hsinchu Science Park, Hsinchu 30076, Taiwan
Prof. D.-Y. Wang
Department of Chemistry
Tunghai University
Taichung 40704, Taiwan
Prof. C.-W. Chen
Center of Atomic Initiative for New Materials (AI-MAT)
National Taiwan University
Taipei 10617, Taiwan
Prof. C.-W. Chen
International Graduate Program of Molecular Science and Technology
National Taiwan University (NTU-MST)
Taipei 10617, Taiwan

DOI: 10.1002/adfm.201902582

© 2019 WILEY-VCH Verlag GmbH & Co. KGaA, Weinheim

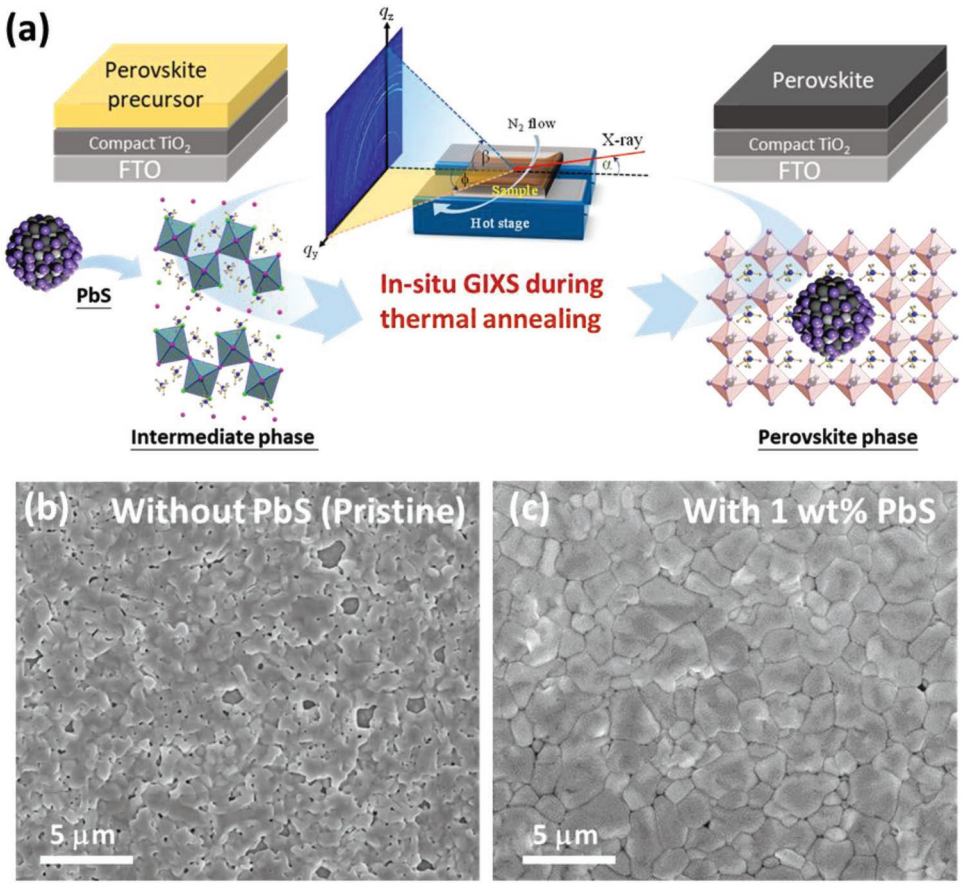

Figure 1. a) Time-resolved GIXS measurement technique to track PbS nanocrystal-assisted growth of perovskite thin films in situ. A moisture-controlled sample chamber was used to simulate the device processing conditions. The SEM morphologies of b) the pristine and c) PbS nanocrystal-seeded (1 wt%) perovskite thin films.

PbS nanoparticles allows the heteroepitaxial growth of thin films with atomically aligned interfaces between PbS nanocrystals (NCs) and the formed perovskite crystals.[10] A similar concept of seeding growth of perovskite thin films, by incorporating submicron-sized crystalline perovskite seeds in the PbI_2 layer during the two-step sequential process, was also reported recently;[12] the perovskite thin films based on this method exhibited a lower trap density, resulting in high-performance perovskite solar cells with excellent durability. Despite the significant progress on the improvement of PCEs in the seeding growth of perovskite solar cells, the roles of seed-like precursor-capped NCs during film growth remain largely speculative, with only information regarding the perovskite film structural features being obtained after postprocessing. As the seeded NCs may alter the perovskite formation routes, a fast in situ observation technique is required to capture the evolution information of the seeding nucleation process of the perovskite crystals assisted by these NCs.[13–15]

In this work, we employed the time-resolved grazing-incidence X-ray scattering (GIXS) technique[5,16] to track PbS NC-assisted growth of perovskite thin films in situ, as shown in **Figure 1**a. With a fast subsecond probing time resolution supported by brilliant synchrotron X-rays, together with a moisture-controlled sample chamber to mimic the device processing conditions, we have unveiled the intermediate structures and the corresponding formation kinetics during conversion to perovskite crystal thin films, assisted by PbS NCs. Through the in situ observation, an important "catalytic" role of the seed-like PbS NCs was clearly elucidated. The perovskite precursor–capped PbS NCs were found to accelerate the nucleation formation of a highly oriented intermediate phase, and subsequently boosted the conversion of the intermediate phase into perovskite crystals with a reduced reaction barrier, compared to that without adding PbS NCs. Our time-resolved GIXS result advances the understanding of the perovskite crystal formation mechanism through the intermediate formation kinetics of NC-assisted nucleation of perovskite crystals,[17,18] leading to substantial morphological improvements in terms of surface coverage, uniformity, and crystallinity of the perovskite films. Our result provides important information for the future development of high-performance organic–inorganic hybrid perovskite solar cells by using perovskite precursor–capped NCs in the seeded growth or chemical additive techniques.[19]

2. Result and Discussion

The solution-processed perovskite thin films of $CH_3NH_3PbI_{3-x}Cl_x$ ($MAPbI_{3-x}Cl_x$) were fabricated using a

© 2019 WILEY-VCH Verlag GmbH & Co. KGaA, Weinheim

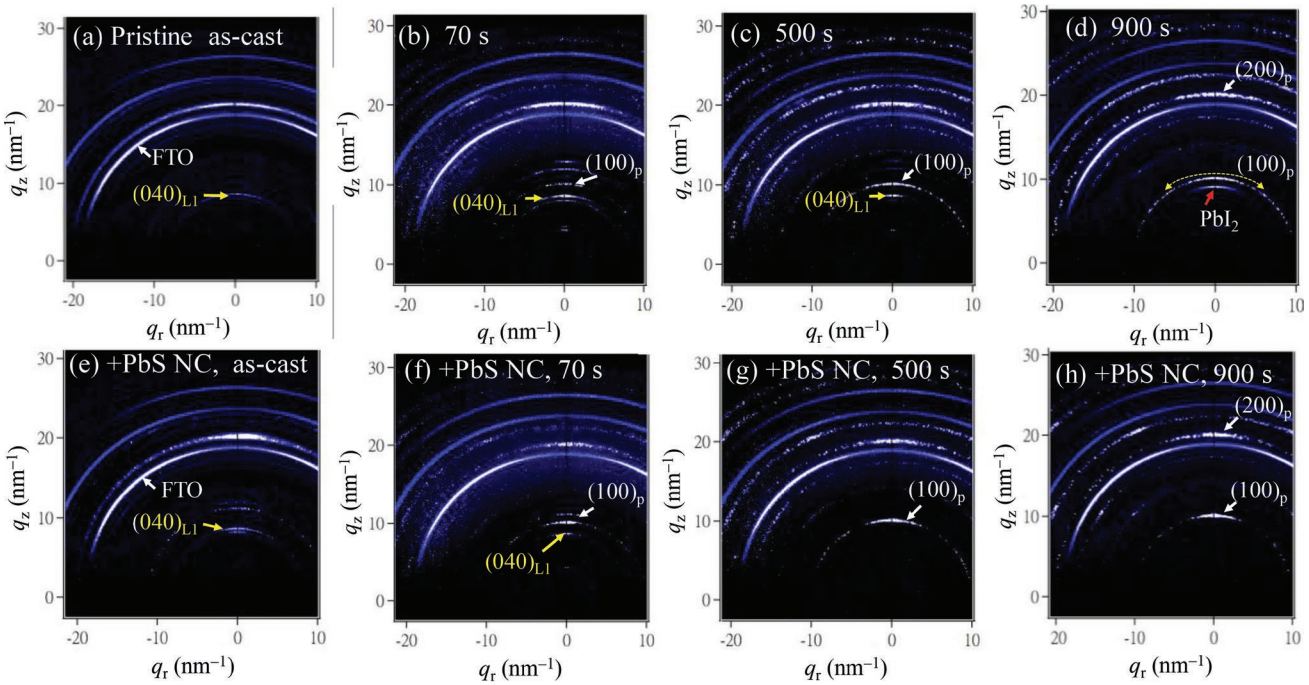

Figure 2. a–d) Representative 2D GIXS patterns of the pristine $MAPbI_{3-x}Cl_x$ perovskite film obtained before (as-cast) and during annealing at 110 °C for the time indicated. The reflections are characterized by $(040)_{L1}$ planes of the intermediate phase $\boldsymbol{L}_1$ and $(100)_p$ and $(200)_p$ of the perovskite cubic crystals. e–h) Evolution of 2D GIXS patterns for PbS NC-seeded (1.0 wt%) perovskite thin film upon annealing at 110 °C. Primary FTO reflections are selectively indicated in (a) and (e). Marked in (d) is the (001) reflection of PbI_2 lamellae. Complete peak assignments are also shown in Figure S2 (Supporting Information).

one-step spin-coating process.[10,20] For the deposition of the perovskite thin films, 40 wt% of MAI/$PbCl_2$ (3:1 in molar ratio) were dissolved in the dimethylformamide (DMF) solvent as a precursor solution. The MAI-capped PbS NCs were prepared following the ligand-exchange treatment reported in our previous work.[10] The typical size of the PbS NCs is ca. 5 nm. These MAI-capped PbS NCs (or PbS NCs hereafter) could be homogeneously dispersed in DMF and were fully compatible with the perovskite precursor for device fabrication. After the spin coating process, the thin films with or without the PbS NCs were annealed at 110 °C in a N_2-purged environment for conversion to the perovskite structure. Figure 1b shows the typical scanning electron microscopic (SEM) morphology of the pristine perovskite thin film (without adding PbS NCs); it comprises relatively randomly and loosely packed perovskite crystals. Some voids and pinholes with sizes ranging from tens to a few hundreds of nm were observed. The corresponding device performance of the pristine perovskite thin film is around 15%. On the contrary, by using a perovskite-precursor solution containing 1 wt% of MAI-capped PbS NCs, the thin film showed a smoother surface morphology consisting of more compact packing and less pinholes and voids of perovskite crystals, as shown in Figure 1c. The resulting solar cell performance significantly improved to over 17%.[10] The detailed device fabrication processes and solar cell characterizations are provided in the Supporting Information.

To further explore the role of PbS NCs on the growth of perovskite thin films, in situ time-resolved GIXS was performed to examine the crystal growth kinetics and the evolution of crystallinity on pristine and PbS NC-seeded perovskite thin films during the thermal annealing process. A detailed instrument setup is described in Figure S1 of the Supporting Information. Samples for the in situ GIXS measurement were spin-coated from the perovskite-precursor solutions with and without PbS NCs on precoated TiO_2/FTO substrates in a N_2-filled glovebox. They were then sealed in a vacuum box and transferred to a GIXS measurement chamber where the moisture was strictly controlled to mimic the environment in the N_2-filled glovebox. The annealing process was then carried out at 110 °C, during which the GIXS patterns were collected at intervals of 500 ms per frame. **Figure 2**a–h shows the representative 2D GIXS patterns of both types of pristine and PbS NC-seeded perovskite thin films at various annealing stages (as-cast, 70, 500, and 900 s). The time-resolved GIXS profiles were obtained along the vertical scatter vector q_z of the corresponding 2D GIXS patterns for both types of pristine and PbS NC-seeded perovskite thin films. **Figure 3**a–f further reveals the detailed evolutions of the corresponding GIXS profiles during the annealing process, indicating that the growth mechanisms are very different. For the pristine thin film, the evolution of perovskite crystallization can be divided into two stages. In the early stage of the first 70 s of the thermal annealing process (Figure 3a), the intensity of the intermediate phase $\boldsymbol{L}_1$ (040) peak centered at $q_z = 8.8$ nm^{-1} gradually increased and became saturated. As identified in our previous work,[21] the $\boldsymbol{L}_1$ phase (of a monoclinic crystal structure with $MA_2PbI_2Cl_2 \cdot MAI$) comprises 2D bilayers of zigzagged octahedra of $[PbI_4Cl_2]^{4-}$ coordination. A schematic of the crystalline features of the $\boldsymbol{L}_1$ phase is also provided in Figure 1a, where iodine ions occupy all the sharing corners and the chlorine ions occupy the terminal corners; the MAI layers are

© 2019 WILEY-VCH Verlag GmbH & Co. KGaA, Weinheim

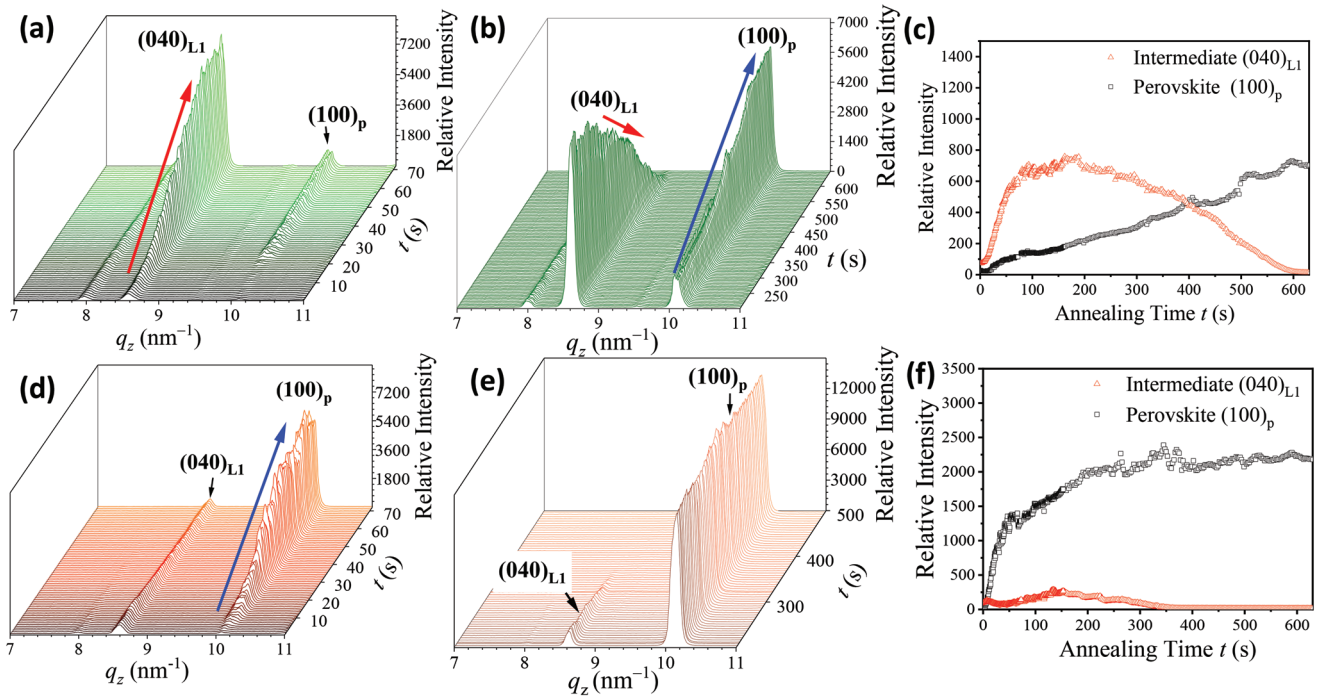

Figure 3. GIXS profiles extracted from the time-resolved 2D GIXS patterns measured during a) the early stage of L_1 formation (first 70 s of annealing) and b) the late stage of L_1-to-perovskite conversion, in 110 °C annealing of the pristine perovskite film. c) Evolutions of the $(040)_{L1}$-integrated peak intensity of L_1 and the perovskite $(100)_p$ peak intensity of the pristine film. d–f) Corresponding results for the 1.0 wt% PbS NC-seeded perovskite thin film.

intercalated between the $[PbI_4Cl_2]^{4-}$ zigzagged octahedra layers (also refer to the Video S1 file in the Supporting Information). Such an intermediate phase of L_1 is mainly associated with enhanced crystal growth kinetics (compared to the direct growth route from precursor to perovskite phase), where the formation of 3D perovskite crystals can be facilitated by interconnecting the 2D-structured octahedra of L_1 intermediate phases.[21] The result can be seen from the progressive conversion of the L_1 phase into the perovskite phase in the later stage of 200–650 s, as shown in Figure 3b, where a gradual diminishing of the (040) reflection at q_z = 8.8 nm^{-1} (red arrow), accompanying a gradually enhanced growth of the (100) reflection of the high-temperature cubic phase of perovskite with the scattering intensity at q = 10.1 nm^{-1} (blue arrow), is clearly observed.[8,18] It took nearly 600 s for the pristine thin film to complete the L_1-to-perovskite conversion during the whole thermal annealing process at 110 °C. It is noted that these GIXS patterns during thermal annealing were captured at 110 °C, at which the dominant phase of perovskite is the cubic phase, with the normal of the reflection planes of $(100)_p$ and $(200)_p$ preferentially aligned to the vertical direction of the film. The cubic phase of the perovskite then transformed to a tetragonal phase after cooling to room temperature, as illustrated in Figure S2 of the Supporting Information. By contrast, the evolution of the GIXS patterns for the PbS NC-seeded perovskite thin film is very different from those of the pristine thin film under the same fabrication conditions. As shown in Figure 3d, although the intermediate phase L_1 also appears at the very early stage of annealing, during the first 70 s for the PbS NC-seeded perovskite thin film, the corresponding scattering intensity centered at q_z = 8.8 nm^{-1} is weak and does not increase with annealing time, compared to that in Figure 3a for the pristine thin film without adding PbS NCs. Most interestingly, the highly oriented (100) peak of the cubic $MAPbI_{3-x}Cl_x$ perovskite crystal centered at q = 10.1 nm^{-1} exhibits a dramatically accelerated growth in the very early stage of annealing, during the first 70 s. At the later stage of 200–650 s, as shown in Figure 3e, the scattering intensity of the (100) peak at q = 10.1 nm^{-1} is nearly constant as a result of saturation formation of the cubic $MAPbI_{3-x}Cl_x$ perovskite crystal. Figure 3c,f summarizes the time evolutions of the integrated peak intensities of both the intermediate phase L_1 at q_z = 8.8 nm^{-1} and the highly oriented $(100)_p$ peak of the cubic $MAPbI_{3-x}Cl_x$ perovskite crystal at q = 10.1 nm^{-1} for the pristine and PbS NC-seeded perovskite thin films, respectively. For the pristine perovskite film, the $(100)_p$ peak intensity of the cubic perovskite only reached 15% of the maximum intensity during the first 70 s before gradually accumulating to the maximum at an annealing time of 600 s. For the PbS NC-seeded perovskite film, the $(100)_p$ peak intensity of the perovskite quickly increased to 60% of the intensity maximum during the first 70 s before asymptotically reaching the intensity maximum at 200 s. The perovskite crystallization rate, hence observed, is much faster when PbS NCs are involved in the L_1-to-perovskite conversion process. We also performed an in situ experiment of the L_1 formation kinetics for both the pristine and PbS NC-seeded perovskite thin films at a lower annealing temperature of 100 °C to capture the slowed down L_1 formation kinetics. As a result, the L_1 formation kinetics was found to be faster by 10 times in the PbS NC-seeded perovskite thin film, compared to that in the pristine film (Figure S3 and Table S1, Supporting Information); this result supports the seeding role of PbS NCs in the L_1-to-perovskite conversion process.

© 2019 WILEY-VCH Verlag GmbH & Co. KGaA, Weinheim

To further quantitatively elucidate the perovskite formation mechanism assisted by PbS nanocrystals, we analyzed the evolution of the integrated peak intensity of the representative perovskite (100) reflection using Avrami analysis,[21,23,24] $\alpha(t) = 1 - \exp\{-[k(t - t_0)]^n\}$, which is often used to describe phase formation kinetics at a constant temperature. The relation can be reduced to a form of Sharp–Hancock presentation with $\ln\{-\ln[1 - \alpha(t)]\} = n \ln(t - t_0) + n \ln(k)$, where the Avrami exponent n and the rate constant k can be determined from the slope and the intercept, respectively, with a properly chosen value of the induction time t_0, as illustrated in **Figure 4**. Typically, $n = 2$ corresponds to accelerated nucleation, while $n = 1$ is sporadic nucleation, assuming no crystal size growth.[21–24] We used the $(100)_p$ integral intensity of the cubic perovskite phase as the representative α in the Avrami analysis. Shown in Figure 4a–c are the temperature-dependent Avrami analyses of the $(100)_p$ cubic perovskite phase for the pristine perovskite and the PbS NC-seeded perovskites with 0.75% and 1.0 wt% PbS NCs, respectively. For each type of perovskite thin film, the growth behaviors at the three designated temperatures of 100, 110, and 120 °C were found to be monotonic and could be fitted by a common n value. For the pristine perovskite thin film, a common Avrami exponent fitted for the three different annealing temperatures is 1.5 ± 0.1 (Figure 4a). The reaction rate constant k values are ≈2.9(±0.2) × 10^{-3} s^{-1} at 100 °C, 5.0(±0.3) × 10^{-3} s^{-1} at 110 °C, and 1.7(±0.2) × 10^{-2} s^{-1} at 120 °C. For the sample consisting of 1.0 wt% PbS NCs, a larger n value of 1.7 ± 0.1 (Figure 4c) indicates an accelerated nucleation behavior.[25] The corresponding reaction rate constant k values, 2.5(±1.1) × 10^{-2} s^{-1} at 100 °C, 3.2(±0.2) × 10^{-2} s^{-1} at 110 °C, and 4.3(±0.7) × 10^{-2} s^{-1} at 120 °C, are almost 1 order of magnitude faster than those of the pristine film at the corresponding temperatures. For the sample consisting of 0.75 wt% PbS NCs (Figure 4b), the n and k values can be found in between (cf. Figure S5 and Table S2, Supporting Information). Furthermore, the corresponding activation energy E_a of the perovskite formation through $\boldsymbol{L}_1$-to-perovskite transformation can be determined from the Arrhenius relation $k(T) \propto \exp[-E_a/(RT)]$, where $k(T)$ is the temperature-dependent Avrami rate constant, T the absolute temperature, and R the gas constant.[21] By fitting the slope $-(E_a/R)$ in Figure 4d, we obtained the activation energies E_a for the perovskite formation via the $\boldsymbol{L}_1$-to-perovskite transformation route of each film, which are E_a = 145 ± 38 (pristine), 112 ± 12 (with 0.75 wt% PbS NCs), and 47 ± 5 (with 1.0 wt% PbS NCs) kJ mol^{-1}, respectively. The activation energy of the PbS NC-seeded perovskite thin films is substantially lowered when PbS nanoparticles are involved in the process of $\boldsymbol{L}_1$-to-perovskite conversion. This result suggests that the PbS NCs may play a "catalytic" role in reducing the energy barrier of the $\boldsymbol{L}_1$-to-perovskite conversion process. In particular, the low activation energy E_a of 47 kJ mol^{-1} for the formation of the PbS NC-seeded perovskite thin film was obtained at the optimum condition with the addition of 1 wt% PbS NCs, consistent with the corresponding best-performance photovoltaic device (Figure S6, Supporting Information). We also estimated the formation energy of the intermediate state $\boldsymbol{L}_1$ from the growth kinetics of the $(040)_{L1}$ reflection, where an activation energy of $E_a \approx 70$ kJ mol^{-1} was found for both the pristine and PbS NC-seeded perovskite thin films (cf. Figure S7, Supporting Information). Figure 4e summarizes the perovskite formation routes without and with the PbS NCs, along the reaction direction. Route **A** represents the pristine thin film without PbS NCs via the dominant $\boldsymbol{L}_1$-to-perovskite conversion and Route **B** represents the perovskite formation with seeded PbS NCs. The activation energy of the $\boldsymbol{L}_1$-to-perovskite conversion was effectively lowered by the addition of 1 wt% MA-capped PbS nanoparticles in the perovskite-precursor film, leading to the dramatically accelerated $\boldsymbol{L}_1$-to-perovskite conversion observed. With increasing concentration of the PbS NCs from 1.0 to 1.5 wt%, the power-conversion efficiency was found to substantially decrease.[10] We also performed in situ GIXS measurement for the sample consisting of 1.5 wt% PbS NCs. The results summarized in Figure S11 (Supporting Information) indicate that a similar reaction mechanism (of the same Avrami exponent n and very similar E_a values) for both the samples consisting of 1.0 and 1.5 wt% PbS NCs; the reaction rate constant k values of the samples consisting of 1.5 wt% PbS NCs were, however, significantly decreased. This may be attributed to aggregation (or segregation) of oversaturated PbS NCs in the film, resulting in significantly reduced film crystallinity and the prominent porous structure observed in our previous work.[10]

A consequence of the PbS-NC accelerated $\boldsymbol{L}_1$-to-perovskite conversion, via a reduced activation energy, may be the improved alignment of perovskite crystals. **Figure 5**a,b shows the evolution of the perovskite crystal orientations of the perovskite $(100)_p$ peak intensity $I(\varphi, t)_{100}$ as a function of the azimuthal angle ψ for the films[26,27] without and with 1.0 wt% PbS NCs, respectively. Although GIXS methodology alone cannot reveal the exact crystal orientation factor due to the missing contribution from perfectly vertically oriented crystals,[28–30] the relatively enhanced orientation of the vertically aligned crystals with a preferential direction perpendicular to the substrate of the film ($\Psi = 90°$) is clearly seen from the PbS NC-seeded sample, compared to the pristine thin film without PbS NCs. The azimuthal GIXS intensities $I(\psi, t)$ of the cubic phase perovskite $(100)_p$ reflection of perovskite exhibited a much narrower distribution width centered at $\Psi = 90°$ in the case of PbS NC-seeded perovskite sample compared to that in the pristine thin film during the formation of perovskite crystals. The result suggests that the inclusion of MAI-capped PbS NCs not only facilitates the nucleation of perovskite by reducing the energy barrier of the $\boldsymbol{L}_1$-to-perovskite conversion process, but also causes the enhanced orientation of vertically aligned crystals with a preferential direction perpendicular to the substrate of the film. Because the transport direction of the photogenerated carriers toward the electrodes is typically perpendicular to the substrate,[18,31] the enhanced orientation of these vertically aligned crystals in the PbS NC-seeded perovskite thin film may therefore lead to a significant improvement in the photovoltaic device performance.[10]

Figure 6 schematically elucidates the role of MAI-capped PbS NCs in the formation of perovskite thin film. First, PbS NCs effectively promote the intermediate route via nucleation formation of the intermediate phase $\boldsymbol{L}_1$. The embedded PbS NCs further provide heteroepitaxial interfaces to accelerate $\boldsymbol{L}_1$-to-perovskite conversion for cubic perovskite crystals of coordinated orientation that can attach to each other for large grains with coherent crystal orientation.[32–34]

© 2019 WILEY-VCH Verlag GmbH & Co. KGaA, Weinheim

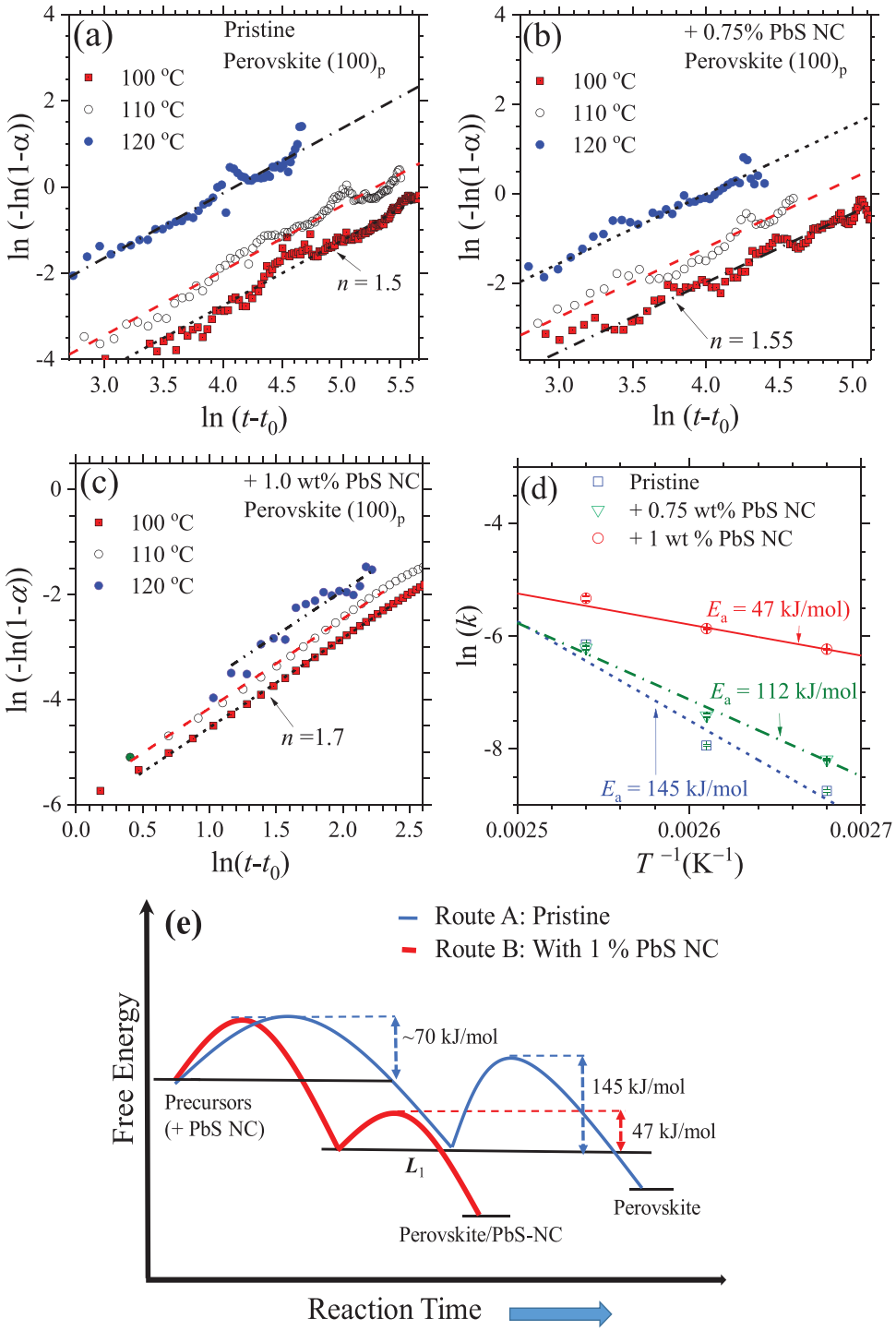

Figure 4. Temperature-dependent evolutions of the integrated peak intensity $\alpha(t)$ of the $(100)_p$ reflection of the cubic perovskite crystal for a) the pristine film, and the films with b) 0.75 wt% and c)1.0 wt% PbS NCs, in the Sharp–Hancock presentation. Data are fitted (dotted lines) with the Avrami exponent n (slopes of the dotted lines) and rate constant $k(T)$ values. d) Arrhenius plots of $k(T)$ with E_a values indicated. e) Routes **A** and **B** along the reaction direction for the pristine perovskite thin film and the PbS NC-seeded perovskite thin film according to E_a values (numbers indicated). Details of the activation energy of the L_1 phase are shown in the Supporting Information.

The corresponding formation process and growth mechanism of the PbS NC-seeded perovskite thin film are further illustrated in the two videos in the Supporting Information, which illustrate how the capped MAI on PbS NCs can promote formation of the L_1 phase (file of Video S1 in the Supporting Information)[35] and how the crystal lattice matched PbS NCs facilitate formation of conjunct and aligned perovskite crystals in a cubic phase (Video S2 file, Supporting Information). Moreover, the

© 2019 WILEY-VCH Verlag GmbH & Co. KGaA, Weinheim

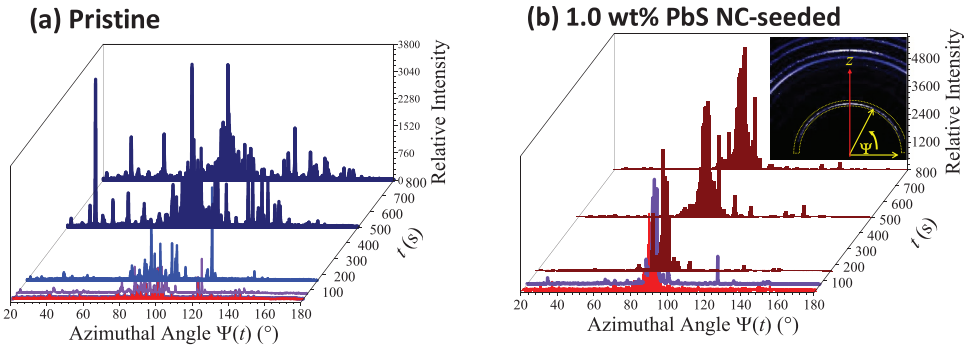

Figure 5. a) Evolutions of the azimuthal GIXS intensity distribution $I(\psi, t)$ of the cubic phase perovskite $(100)_p$ reflection of the perovskite films with a) 0% (pristine) and b) 1.0 wt% PbS NCs, measured during annealing at 110 °C.

proposed epitaxial growth of the $MAPbI_{3-x}Cl_x$ crystals centered on the PbS NCs is evidenced by the high-resolution transmission electron microscopy (HRTEM) image in **Figure 7**, showing a PbS NC (of cubic lattice parameter 5.97 Å) lattice-aligned with the surrounded $MAPbI_{3-x}Cl_x$ crystals. The $(11\bar{1})$ planes of the PbS NC (0.35 nm in spacing) are clearly observed, with the neighboring (400) planes (0.22 nm in spacing) of the tetragonal $MaPbI_{3-x}Cl_x$ matrix. Specifically, the plane normal of the $MaPbI_{3-x}Cl_x$ perovskite (400) planes is parallel to the $(02\bar{2})$ reciprocal lattice vector of the PbS NC, suggesting that the (400) planes are parallel to the $(02\bar{2})$ planes of the PbS NC. Such heterogeneous crystal interface alignment would enhance the film texture (Figure 2) of the perovskite film embedded with the PbS NCs. This is similar to the "dots-in-a-matrix" crystals consisting of atomically aligned interfaces of PbS NCs within a $MAPbI_3$ perovskite matrix, illustrated in previous reports.[19,36] Accordingly, we attribute the significantly larger grain sizes of the PbS-seeded perovskite film shown in Figure 1 to better packed and lattice-aligned perovskite crystals around the PbS NC seed. We note that the crystal size of the PbS NC-seeded perovskite monitored by GIXS along an in situ reaction is in general smaller than that of the pristine film (Figure S4, Supporting Information), which is a consequence of the much faster nucleation kinetics of the perovskite crystal formation with PbS NCs.

Through lattice-aligned heterointerfaces, the PbS NC-seeded perovskite thin film also exhibited enhanced thermal stability compared to the pristine perovskite thin film. As we performed prolonged annealing at 110 °C for 1000 s for both the pristine and PbS NC-seeded perovskite thin films (**Figure 8**), a much stronger PbI_2 peak (q = 9.1 nm^{-1}) in the GIXS profiles was observed as a result of the decomposition of perovskite crystals in the pristine perovskite thin film as compared to that in the PbS NC-seeded one.[31] Improved thermal stability with weaker decay of the peak intensity of the perovskite crystals at elevated annealing temperature was also observed for the PbS NC-seeded perovskite thin film, as compared to that in the pristine perovskite thin film (Figure S8, Supporting Information). The enhanced thermal stability of the perovskite crystals through lattice anchoring to the PbS NCs reported here would be of particular advantages in considerably long high-temperature annealing for the cubic α-phase of the high-performance perovskite solar cells with mixed cations of Cs^+, $CH(NH_2)_2^+$

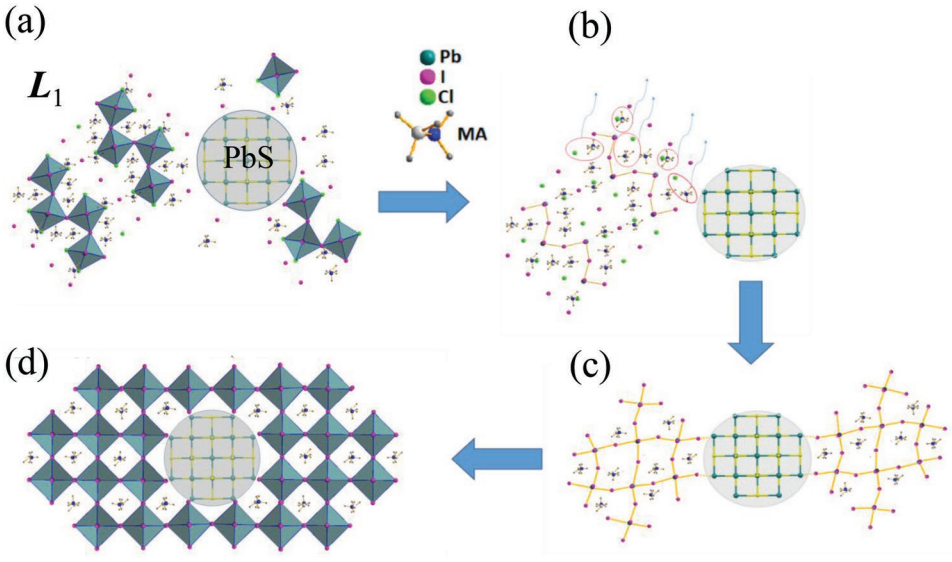

Figure 6. Schematics for the formation of $MAPbI_{3-x}Cl_x$ perovskite seeded by a PbS NC, starting from a) accelerated formation of the L_1 phase by the heterointerfaces with the MAI-capped PbS NC, followed by b) MACl formation and sublimation. c) Subsequent L_1-to-pervoskite conversion facilitated by perovskite lattice alignment with the cubic lattice of the PbS NC. d) Closely packed and lattice-aligned perovskite crystals centered around the PbS NC.

© 2019 WILEY-VCH Verlag GmbH & Co. KGaA, Weinheim

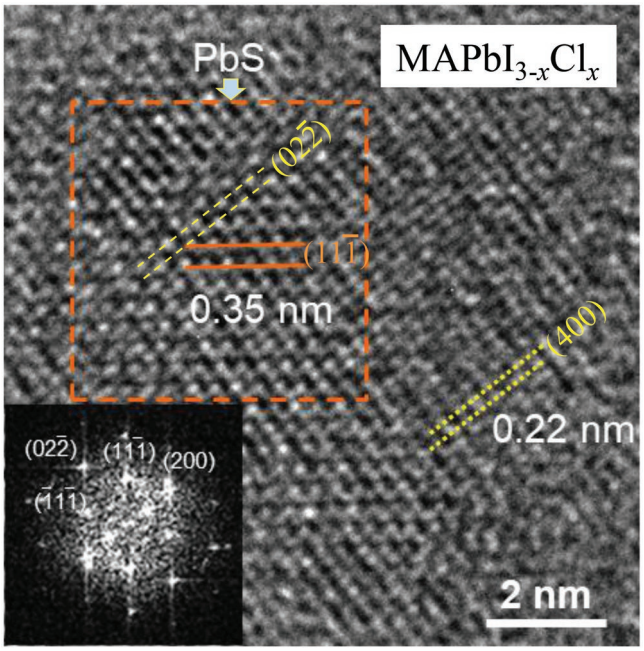

Figure 7. HRTEM image showing a PbS nanocrystal embedded in the $MAPbI_{3-x}Cl_x$ matrix. The inset shows the fast Fourier transform (FFT) over the PbS NC region within the dashed square. The FFT pattern has the same symmetry as the [011] zone axis pattern of the face-centered cubic PbS lattice, with the indices of the reciprocal lattice points labeled accordingly. The (11$\bar{1}$) and (02$\bar{2}$) lattice planes of the PbS NC are indicated by a pair of solid orange lines (of 0.35 nm spacing) and dashed yellow lines, and the (400) lattice planes of the tetragonal phase of $MaPbI_3$ are indicated by a pair of dotted yellow lines (of 0.22 nm spacing). The HRTEM image was taken using a JEOL AEM 2010F system, operated at 200 kV.

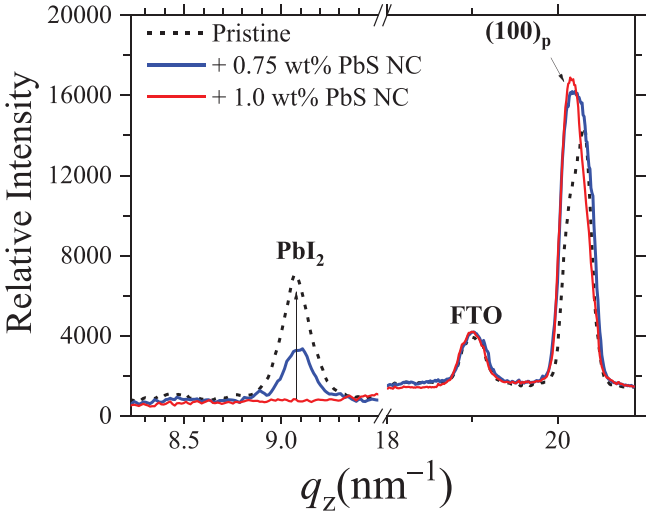

Figure 8. GIXS profiles for a pristine perovskite film and PbS NC-seeded perovskite thin films with respectively 0.75 and 1.0 wt% of PbS NCs measured upon prolonged annealing (≈1000 s) at 110 °C. The stronger PbI_2 peak (at $q \approx 9.1$ nm^{-1}) from decomposition of perovskite crystals in the pristine film suggests a lower thermal stability.

(FA), and MA^+.[37,38] The photoactive α phase of $FA_xMA_{1-x}PbI_3$ is known to transit relatively easily to the photoinactive yellow orthorhombic δ phase at room temperature.[39,40] Indeed, a similar lattice anchoring effect of PbS nanoparticles was reported (parallel to this study) to impressively enhance the stability of the cubic phase of cesium lead halide perovskites.[36]

The above analyses of the temperature-dependent and time-resolved crystal formation kinetics obtained from the X-ray results reveal dual functions of the PbS nanocrystals, including accelerating the nucleation of the intermediate L_1 phase and the subsequent catalyzing the intermediate phase into perovskite crystals. The first function is associated with the hetero-interfaces provided by the MAI-capped PbS NCs that could facilitate localization of $[PbI_6]^{4-}$ octahedra for accelerated and orientated L_1 phase formation. The second function of the seed-like PbS nanocrystals is to catalyze the conversion of the L_1 phase into the cubic phase of the $MAPbI_{3-x}Cl_x$ perovskite via lattice alignment. On the basis of the comparable sizes of the L_1 phase and the perovskite crystals observed along the reaction (cf. Figures S4 and S7, Supporting Information), the intermediate L_1 phase can be regarded as the nuclei of the perovskite formation via L_1-to-perovskite transition. In this scenario, PbS NCs reduce the activation energy of the L_1-to-perovskite transition (Figure 4). The hence formed perovskite nanocrystals are better packed and aligned into larger and ordered grains, leading to a smoother and more homogeneous (Figure S9, Supporting Information) film morphology with less pinholes and enhanced crystal texture and thermal stability. Correspondingly observed are the enhanced charge transport[10] and the PCE value of the perovskite film with PbS NCs (Figures S6 and S10, Supporting Information). We note that the selection strategy of perovskite additives for improving perovskite solar cell performance through different aspects were detailed in recent reports.[38,41–43]

3. Conclusions

In conclusion, we have unveiled the nucleation kinetics of PbS NC-seeded perovskite thin films by time-resolved GIXS. The MAI-capped PbS NCs were found to play a catalytic role to promote the nucleation formation of the highly oriented intermediate phase L_1 and reduce the energy barrier of the L_1-to-perovskite conversion. The PbS NC-seeded perovskite thin film exhibited enhanced crystallinity, crystal orientation, and thermal stability, together with the refined film morphology of reduced pinholes and grain boundaries, compared to the pristine thin film. All the elucidated effects of the PbS nanocrystals provide hints for the future design on seeding growth of perovskite thin films or a heterointerface-enhanced performance of halide perovskite solar cells,[44] by taking into account the crystal lattice matching and ligand surfaces of the nanocrystals.

4. Experimental Section

Sample Preparation: MAI-capped PbS nanocrystals were prepared following that reported previously[10] and were dispersed in dimethylformamide then added to the perovskite-precursor solutions (40 wt% of MAI and PCl_2 in 3:1 molar ratio in DMF) of 0, 0.75, and 1.0 wt% PbS NCs, with respect to the total weight of the perovskite precursors. Perovskite-precursor thin films were spin-coated from the

© 2019 WILEY-VCH Verlag GmbH & Co. KGaA, Weinheim

DMF mixtures onto FTO glass substrates (14×14 mm^2) precoated with a compact TiO_2 layer (≈200 nm in thickness). The prepared perovskite-precursor thin films were ≈350 nm in thicknesses.

Grazing-Incidence X-Ray Scattering: In situ GIXS was conducted at the 23A SWAXS beamline of the Taiwan Light Source of the National Synchrotron Radiation Research Center, Hsinchu.[45] The perovskite-precursor thin films were positioned respectively on a heating stage in a vacuum-tight chamber with flowing N_2 for annealing at 100, 110, or 120 °C (Figure S1, Supporting Information). With a 15 keV X-ray beam at 2.0° incidence and a sample-to-detector distance of 186.0 mm, GIXS data were collected with 500 ms in the first ≈70 s of annealing, followed by 1 s time-resolution in the later stage of annealing, using a CMOS flat panel detector C10158DK-3957 (active area 10×10 cm^2). The scattering peak positions were calibrated rigorously using the diffraction peaks from powders of Si, Ag-behenate, and LaB_6. The in-plane and out-of-plane scattering vector are respectively defined by q_r and q_z, with $q_r = (q_x^2 + q_y^2)^{1/2}$, as detailed in Figure S1 (Supporting Information).[46]

Supporting Information

Supporting Information is available from the Wiley Online Library or from the author.

Acknowledgements

C.-Y.L. and S.-S.L. contributed equally to this work. The authors thank the assistance of Dr. C.-M. Chou in photoluminescence measurements. Discussion with Dr. O. Shih is acknowledged. This work was supported by Minster of Science and Technology (MOST), Taiwan and Taiwan Consortium of Emergent Crystalline Materials (TCECM) (Project Nos. 107-2119-M-002-028-MY2, 107-2112-M-002-024-MY3, 105-2112-M-038-001-MY3, and 105-2112-M-213-010-MY3). Financial support by Taipei Medical University (DP2-108-21121-01-O-06-02 and TMU107-AE1-B10), the Center of Atomic Initiative for New Materials, National Taiwan University, and the Featured Areas Research Center Program within the framework of the Higher Education Sprout Project by the Ministry of Education in Taiwan (108L9008) is acknowledged.

Conflict of Interest

The authors declare no conflict of interest.

Keywords

catalytic additives, grazing-incidence X-ray scattering, heterogeneous interface, organo-lead trihalide perovskite, PbS nanocrystals

Received: March 29, 2019
Revised: June 6, 2019
Published online: July 4, 2019

[1] M. Saliba, T. Matsui, K. Domanski, J. Y. Seo, A. Ummadisingu, S. M. Zakeeruddin, J. P. Correa-Baena, W. R. Tress, A. Abate, A. Hagfeldt, M. Grätzel, *Science* **2016**, *354*, 206.
[2] X. Li, D. Bi, C. Yi, J.-D. Décoppet, J. Luo, S. M. Zakeeruddin, A. Hagfeldt, M. Grätzel, *Science* **2016**, *353*, 58.
[3] M. Saliba, J.-P. Correa-Baena, M. Grätzel, A. Hagfeldt, A. Abate, *Angew. Chem., Int. Ed.* **2018**, *57*, 2554.
[4] J.-P. Correa-Baena, M. Saliba, T. Buonassisi, M. Grätzel, A. Abate, W. Tress, A. Hagfeldt, *Science* **2017**, *358*, 739.
[5] A. T. Barrows, S. Lilliu, S. A. J. Pearson, D. Babonneau, A. D. F. Dunbar, D. G. Lidzey, *Adv. Funct. Mater.* **2016**, *26*, 4934.
[6] N. J. Jeon, J. H. Noh, Y. C. Kim, W. S. Yang, S. Ryu, S. I. Seok, *Nat. Mater.* **2014**, *13*, 897.
[7] J. Kim, T. Hwang, S. Lee, B. Lee, J. Kim, G. S. Jang, S. Nam, B. Park, *Sci. Rep.* **2016**, *6*, 25648.
[8] B. J. Foley, J. Girard, B. A. Sorenson, A. Z. Chen, S. J. Niezgoda, M. R. Alpert, A. F. Harper, D.-M. Smilgies, P. Clancy, W. A. Saidie, J. J. Choi, *J. Mater. Chem. A* **2017**, *5*, 113.
[9] Y. Chen, M. He, J. Peng, Y. Sun, Z. Liang, *Adv. Sci.* **2016**, *3*, 1500392.
[10] S.-S. Li, C.-H. Chang, Y.-C. Wang, C.-W. Lin, D.-Y. Wang, J.-C. Lin, C.-C. Chen, H.-S. Sheu, H.-C. Chia, W.-R. Wu, U. Jeng, C.-T. Liang, R. Sankar, F.-C. Chou, C.-W. Chen, *Energy Environ. Sci.* **2016**, *9*, 1282.
[11] P. W. Liang, C. Y. Liao, C. C. Chueh, F. Zuo, S. T. Williams, X. K. Xin, J. Lin, A. K. Jen, *Adv. Mater.* **2014**, *26*, 3748.
[12] Y. Zhao, H. Tan, H. Yuan, Z. Yang, J. Z. Fan, J. Kim, O. Voznyy, O. Gong, L. A. Quan, C. S. Tan, J. Hofkens, D. Yu, Q. Zhao, E. H. Sargent, *Nat. Commun.* **2018**, *9*, 1607.
[13] Q. Hu, L. Zhao, J. Wu, K. Gao, D. Luo, Y. Jiang, Z. Zhang, C. Zhu, E. Schaible, A. Hexemer, C. Wang, Y. Liu, W. Zhang, M. Grätzel, F. Liu, T. P. Russell, R. Zhu, Q. Gong, *Nat. Commun.* **2017**, *8*, 15688.
[14] B.-A. Chen, J.-T. Lin, N.-T. Suen, C.-W. Tsao, T.-C. Chu, Y.-Y. Hsu, T.-S. Chan, Y.-T. Chan, J.-S. Yang, C.-W. Chiu, H. M. Chen, *ACS Energy Lett.* **2017**, *2*, 342.
[15] P. K. Nayak, D. T. Moore, B. Wenger, S. Nayak, A. A. Haghighirad, A. Fineberg, N. K. Noel, O. G. Reid, G. Rumbles, P. Kukura, K. A. Vincent, H. J. Snaith, *Nat. Commun.* **2016**, *7*, 13303.
[16] C. Zhu, X. Niu, Y. Fu, N. Li, C. Hu, Y. Chen, X. He, G. Na, P. Liu, H. Zai, Y. Ge, Y. Lu, X. Ke, Y. Bai, S. Yang, P. Chen, Y. Li, M. Sui, L. Zhang, H. Zhou, Q. Chen. *Nat. Commun.* **2019**, *10*, 815.
[17] B. Wang, K. Y. Wong, X. Xiao, T. Chen, *Sci. Rep.* **2015**, *5*, 10557.
[18] A. Z. Chen, B. J. Foley, J. H. Ma, M. R. Alpert, J. S. Niezgoda, J. J. Choi, *J. Mater. Chem. A* **2017**, *5*, 7796.
[19] Z. Ning, X. Gong, R. Comin, G. Walters, F. Fan, O. Voznyy, E. Yassitepe, A. Buin, S. Hoogland, E. H. Sargent, *Nature* **2015**, *523*, 324.
[20] Q. Dong, Y. Yuan, Y. Shao, Y. Fang, Q. Wang, J. Huang, *Energy Environ. Sci.* **2015**, *8*, 2464.
[21] H.-C. Chia, H.-S. Sheu, Y.-Y. Hsaio, S.-S. Li, Y.-K. Lan, C.-Y. Lin, J.-W. Chang, Y.-C. Kuo, C.-H. Chen, S.-C. Weng, C.-J. Su, A.-C. Su, C.-W. Chen, U. Jeng, *ACS Appl. Mater. Interfaces* **2017**, *9*, 36897.
[22] J. L. Allen, T. R. Jow, J. Wolfenstine, *Chem. Mater.* **2007**, *19*, 2108.
[23] D. T. Moore, H. Sai, K. W. Tan, D.-M. Smilges, W. Zhang, H. J. Snaith, U. Wiesner, L. A. Estroff, *J. Am. Chem. Soc.* **2015**, *137*, 2350.
[24] W.-R. Wu, U. Jeng, C.-J. Su, K.-H. Wei, M.-S. Su, M.-Y. Chiu, C.-Y. Chen, W.-B. Su, C.-H. Su, A.-C. Su, *ACS Nano* **2011**, *5*, 6233.
[25] A. Ummadisingu, L. Steier, J.-Y. Seo, T. Matsui, A. Abate, W. Tress, M. Grätzel, *Nature* **2017**, *545*, 208.
[26] J. Rivnay, S. C. B. Mannsfeld, C. E. Miller, A. Salleo, M. F. Toney, *Chem. Rev.* **2012**, *112*, 5488.
[27] W.-R. Wu, C.-J. Su, W. T. Chuang, Y.-C. Huang, P.-W. Yang, P.-C. Lin, C.-Y. Chen, T.-Y. Yang, A.-C. Su, K.-H. Wei, C.-M. Liu, U. Jeng, *Adv. Energy Mater.* **2017**, *7*, 1601842.
[28] J. L. Baker, L. H. Jimison, S. Mannsfeld, S. Volkman, S. Yin, V. Subramanian, A. Salleo, A. P. Alivisatos, M. F. Toney, *Langmuir* **2010**, *26*, 9146.
[29] J. L. White, J. E. Spruiell, *Polym. Eng. Sci.* **1983**, *23*, 247.
[30] J. Schlipf, P. Müller-Buschbaum, *Adv. Energy Mater.* **2017**, *7*, 1700131.

© 2019 WILEY-VCH Verlag GmbH & Co. KGaA, Weinheim

[31] V. L. Pool, B. Dou, D. G. Van Campen, T. R. Klein-Stockert, F. S. Barnes, S. E. Shaheen, M. I. Ahmad, M. F. A. M. van Hest, M. F. Toney, *Nat. Commun.* **2017**, *8*, 4075.
[32] K. A. Bush, N. Rolston, A. Gold-Parker, S. Manzoor, J. Hausele, Z. J. Yu, J. A. Raiford, R. Cheacharoen, Z. C. Holman, M. F. Toney, R. H. Dauskard, M. D. McGehee, *ACS Energy Lett.* **2018**, *3*, 1225.
[33] A. Ummadisingu, M. Grätzel, *Sci. Adv.* **2018**, *4*, e1701402.
[34] T. S. Sherkar, C. Momblona, L. Gil-Escrig, J. Ávila, M. Sessolo, H. J. Bolink, L. J. A. Koster, *ACS Energy Lett.* **2017**, *2*, 1214.
[35] K. H. Stone, A. Gold-Parker, A. L. Pool, E. L. Unger, A. R. Bowring, M. D. McGehee, M. F. Toney, C. J. Tassone, *Nat. Commun.* **2018**, *9*, 3458.
[36] M. Liu, Y. Chen, C.-S. Tan, R. Quintero-Bermudez, A. H. Proppe, R. Munir, H. Tan, O. Voznyy, B. Scheffel, G. Walters, A. P. T. Kam, B. Sun, M.-J. Choi, S. Hoogland, A. Amassian, S. O. Kelley, F. P. García de Arquer, E. H. Sargent, *Nature* **2019**, *570*, 96.
[37] G. Zheng, C. Zhu, J. Ma, X. Zhang, G. Tang, R. Li, Y. Chen, L. Li, J. Hu, J. Hong, Q. Chen, X. Gao, H. Zhou, *Nat. Commun.* **2018**, *9*, 2793.
[38] L. K. Ono, E. J. Juarez-Perez, Y. Qi, *ACS Appl. Mater. Interfaces* **2017**, *9*, 30197.
[39] J.-P. Correa-Baena, A. Abate, M. Saliba, W. Tress, T. J. Jacobsson, M. Grätzel, A. Hagfeldta, *Energy Environ. Sci.* **2017**, *10*, 710.
[40] S. Yuan, F. Qian, S. Yang, Y. Cai, Q. Wang, J. Sun, Z. Liu, S. F. Liu, *Adv. Funct. Mater.* **2019**, https://doi.org/10.1002/adfm.201807850.
[41] J.-W. Xiao, S. Ma, S. Yu, C. Zhou, P. Liu, Y. Chen, H. Zhou, Y. Li, Q. Chen, *Nano Energy* **2018**, *46*, 45.
[42] T. Li, Y. Pan, Z. Wang, Y. Xia, Y. Chen, W. Huang, *J. Mater. Chem. A* **2017**, *5*, 12602.
[43] L. Liu, S. Huang, Y. Lu, P. Liu, Y. Zhao, C. Shi, S. Zhang, J. Wu, H. Zhong, M. Sui, H. Zhou, H. Jin, Y. Li, Q. Chen, *Adv. Mater.* **2018**, *30*, 1800544.
[44] P. Schulz, D. Cahen, A. Kahn, *Chem. Rev.* **2019**, *119*, 3349.
[45] U. Jeng, C.-H. Su, C.-J. Su, K.-F. Liao, W.-T. Chuang, Y.-H. Lai, Y.-J. Chang, Y.-J. Chen, Y.-S. Huang, M.-T. Lee, K.-L. Yu, J.-M. Lin, D.-G. Liu, C.-F. Chang, C.-Y. Liu, C.-H. Chang, K. S. Liang, *J. Appl. Crystallogr.* **2010**, *43*, 110.
[46] Z. Jiang, *J. Appl. Crystallogr.* **2015**, *48*, 917.

© 2019 WILEY-VCH Verlag GmbH & Co. KGaA, Weinheim